Optical antenna design for fluorescence enhancement in the ultraviolet

Xiaojin Jiao and Steve Blair*

Department of Electrical and Computer Engineering, University of Utah
Salt Lake City, UT, 84112, USA

*blair@ece.utah.edu

http://photonics.ece.utah.edu

Abstract: Through rational design, we compare the performance of three plasmonic antenna structures for UV fluorescence enhancement. Among the antenna performance metrics considered are the local increase in excitation intensity and the increase in quantum efficiency, the product of which represents the net fluorescence enhancement. With realistic structures in aluminum, we predict that greater than 100× net enhancement can be obtained.

OCIS codes: (240.6680) Surface plasmons; (300.6540) Spectroscopy, ultraviolet.

References and links

1. R. F. Chen "Fluorescence quantum yields of tryptophan and tyrosine," Anal. Lett. **1,** 35–42 (1967).
2. C. R. Johnson, M. Ludwig, S. O'Donnell, and S. A. Asher "UV resonance Raman spectroscopy of the aromatic amino acids and myoglobin," J. Am. Chem. Soc. **106,** 5008–5010 (1984).
3. G. D. Fasman, ed. *Practical Handbook of Biochemistry and Molecular Biology*. CRC Press 1989.
4. K. Ray, M. H. Chowdhury, and J. R. Lakowicz "Aluminum nanostructured films as substrates for enhanced fluorescence in the ultraviolet-blue spectral region," Anal. Chem. **79,** 6480–6487 (2007).
5. H. Szmacinski, K. Ray, and J. R. Lakowicz "Metal-enhanced fluorescence of tryptophan residues in proteins: Application towards label-free bioassays," Anal. Biochem. **385,** 358–364 (2008).
6. J. R. Lakowicz, B. Shen, Z. Gryczynski, S. D'Auria, and I. Gryczynski "Intrinsic fluorescence from DNA can be enhanced by metallic particles," Biochem. Biophys. Res. Commun. **286,** 875–879 (2001).
7. J. R. Lakowicz, J. Malicka, I. Gryczynski, Z. Gryczynski, and C. D. Geddes "Radiative decay engineering: the role of photonic mode density in biotechnology," J. Phys. D: Appl. Phys. **36,** R240–R249 (2003).
8. K. Aslan, M. J. R. Previte, Y. Zhang, and C. D. Geddes "Surface plasmon coupled fluorescence in the ultraviolet and visible spectral regions using zinc thin films," Anal. Chem. **80,** 7304–7312 (2008).
9. A. Kinkhabwala, Z. Yu, S. Fan, Y. Avlasevich, K. Müllen, and W. E. Moerner "Large single-molecule fluorescence enhancements produced by a bowtie nanoantenna," Nat. Photonics **3,** 654–657 (2009).
10. A. Taguchi, N. Hayazawa, K. Furusawa, H. Ishitobi, and S. Kawata "Deep-UV tip-enhanced raman scattering," J. Raman Spectrosc. **40,** 1324–1330 (2009).
11. C. C. Davis "Fluorescence: Molecules in a tight spot," Nat. Photonics **3,** 608–609 (2009).
12. S. Attavar, M. Diwekar, and S. Blair "Photoactivated capture molecule immobilization in plasmonic nanoapertures in the ultraviolet," Lab Chip **11,** 841–844 (2011).
13. M. T. Neves-Petersen, T. Snabe, S. Klitgaard, M. Duroux, and S. B. Petersen "Photonic activation of disulfide bridges achieves oriented protein immobilization on biosensor surfaces," Protein Sci. **15,** 343–351 (2006).
14. K. Aslan and C. D. Geddes "Directional surface plasmon coupled luminescence for analytical sensing applications: Which metal, what wavelength, what observation angle?," Anal. Chem. **81,** 6913–6922 (2009).
15. P. R. West, S. Ishii, G. V. Naik, N. K. Emani, V. M. Shalaev, and A. Boltasseva "Searching for better plasmonic materials," Laser & Photon. Rev. **4,** 795–808 (2010).
16. S. Blair and J. Wenger "Enhancing fluorescence with sub-wavelength metallic apertures," in *The Role of Plasmonic Engineering in Surface-Enhanced Fluorescence* (C. D. Geddes, ed.) ch. 17 John Wiley & Sons 2008.
17. E. M. Purcell "Spontaneous emission probabilities at radio frequencies," Phys. Rev. **69,** 681 (1946).
18. H. Aouani, O. Mahboub, N. Bonod, E. Devaux, E. Popov, H. Rigneault, T. W. Ebbesen, and J. Wenger "Bright unidirectional fluorescence emission of molecules in a nanoaperture with plasmonic corrugations," Nano Lett. **11,** 637–644 (2011).

#175459 - $15.00 USD Received 6 Sep 2012; revised 30 Nov 2012; accepted 1 Dec 2012; published 21 Dec 2012

19. F. Mahdavi and S. Blair "Nanoaperture fluorescence enhancement in the ultraviolet," Plasmonics **5,** 169–174 (2010).
20. E. D. Palik, "*Handbook of Optical Constants of Solids*," Academic Press, London (1985)
21. L. Novotny and B. Hecht, "*Principles of Nano-Optics*," Cambridge University Press, Cambridge, (2006).
22. H. Fischer and O. J. F. Martin "Engineering the optical response of plasmonic nanoantennas," Opt. Express **16,** 9144–9154 (2008).
23. O. Mahboub, S. C. Palacios, C. Genet, F. J. Garcia-Vidal, S. G. Rodrigo, L. Martin-Moreno, and T. W. Ebbesen "Optimization of bull's eye structures for transmission enhancement," Opt. Express **18,** 11292–11299 (2010).
24. M. Kuttge, F. J. G. de Abajo, and A. Polman "How grooves reflect and confine surface plasmon polaritons," Opt. Express **17,** 10385–10392 (2009).
25. S. Carretero-Palacios, O. Mahboub, F. J. Garcia-Vidal, L. Martin-Moreno, S. G. Rodrigo, C. Genet, and T. W. Ebbesen "Mechanisms for extraordinary optical transmission through bull's eye structures," Opt. Express **19,** 10429–10442 (2011).
26. H. J. Lezec, A. Degiron, E. Devaux, R. A. Linke, L. Martin-Moreno, F. J. Garvia-Vidal, and T. W. Ebbesen "Beaming light from a subwavelength aperture," Science **297,** 820–822 (2002).

1. Introduction

The field of plasmonics has been primarily focused on the visible-NIR range, with comparatively little effort devoted to the UV (defined here as $\lambda < 400$ nm). Motivating factors in the study of UV plasmonics are the direct access to biomolecular resonances and native fluorescence, resonant Raman scattering interactions, and the potential for exerting control over photochemical reactions, including photocatalysis.

Organic molecules have electronic resonances in the UV part of the spectrum. The advantages of UV-resonant molecular spectroscopy have been recognized for decades [1, 2], such as the use of UV resonant Raman scattering for structural conformational and kinetics studies. Biomolecules such as peptides and proteins contain residues that absorb in the UV (220-280 nm); the aromatic amino acids tryptophan, tyrosine, and phenylalanine are fluorescence and Raman active. However, aromatic residues have relatively low fluorescence quantum efficiencies and molar extinction coefficients [1, 3], as do nucleic acid bases, so achieving significant enhancement via plasmonic structures [4] could be a key enabling factor in the label-free detection of proteins [5] or DNA molecules [6, 7]. Label-free detection methods are highly desirable for the measurement of the kinetics of molecular interactions, which, when implemented in a highly-parallel manner, enable mapping of the interactome of biological systems. Nevertheless, there are numerous organic dye labels in use that absorb/fluoresce in the UV [8]

For native fluorescence, "brightness" (which is the product of absorption cross-section and quantum efficiency) is about $100\times$ lower than for common fluorescent dyes in the visible. Therefore, a metric goal for UV optical antenna design is obtaining $\sim 100\times$ fluorescent enhancement, which is clearly possible in the visible [9], but not demonstrated in the UV. For comparison, UV resonant Raman cross-sections of many biomolecules are comparable to resonant cross-sections of organic dye molecules; UV resonance results in approximately a 10^5 increase in cross-section as compared to non-resonant excitation conditions [2]. Indeed, tip-enhanced UV resonance Raman scattering has been demonstrated [10].

Photochemical reactions can be exploited in the UV, where plasmonic enhancement can be used to drive localized chemical reactions on a scale commensurate with the molecules themselves [11] and with increased reaction rates [12]. For example, when aromatic residues in proteins are in proximity to disulphide bonds, $\sim$280 nm irradiation of the residue can induce breakage of the disulphide bond, creating free thiol groups that link with thiol-reactive surfaces such as Au [13]. Other reactive groups can be used for photocrosslinking at wavelengths typically near 365 nm, such as aryl azides, benzophenone, diazirine rings, and anthraquinones.

One of the limiting factors for UV plasmonics is the material response. Conventional "plasmonic" metals such as Ag and Au suffer from the influence of interband transitions near the

#175459 - $15.00 USD Received 6 Sep 2012; revised 30 Nov 2012; accepted 1 Dec 2012; published 21 Dec 2012

blue part of the spectrum, whereas the interband transition for Al lies in the near infrared, opening up a near Drude-like response in the UV. Other metals are suitable for UV plasmonic applications [14]. Fig. 1 plots the SPP and LSPR "quality factors" [15], or figures of merit, for some common metals. Clearly, of the metals considered, Al has the highest quality factor in the UV, and is the metal chosen for this study.

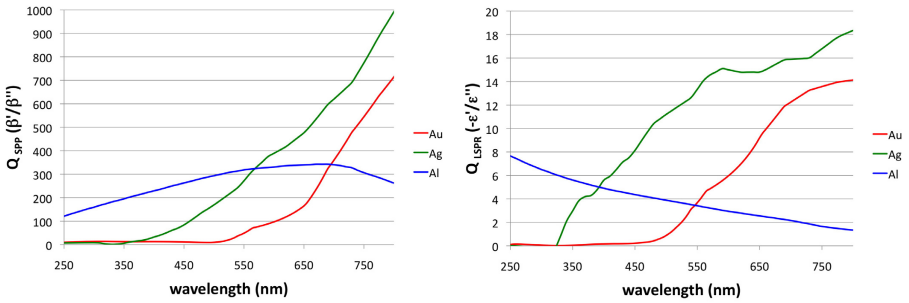

(a) (b)

Fig. 1. Plots of SPP (a) and LSPR (b) quality factors for three different metals. The quality factors for Ag and Au drop significantly at short wavelengths due to interband transitions.

This paper focuses on native fluorescence enhancement as an exemplary application of UV plasmonics, but the results apply to other applications as well. Therefore, we compare UV fluorescence enhancement using three canonical plasmonic structures - dipole antenna, bull's eye nanoaperture and nanoaperture array.

2. Simulation model

Most fluorescent molecules can be treated as a system of three energy levels—singlet ground state S_0, first excited singlet state S_1, and dark non-fluorescing, or first excited triplet state T_1. The fluorescence count rate per molecule (CRM) in steady state is given by [16]

$$CRM = \kappa\phi\frac{\sigma I_e}{1+I_e/I_s} \tag{1}$$

where κ is the light collection efficiency (combination of the optical system and radiation profile), $\phi = k_{rad}/k_{tot}$ the quantum efficiency (QE), k_{rad} and k_{nr} the rate constants for radiative emission and non-radiative de-excitation from S_1 to S_0, $k_{tot} = k_{rad} + k_{nr}$ the inverse of the excited state lifetime τ, σI_e the net excitation rate, σ the absorption cross-section, and the saturation intensity $I_s = k_{tot}/[\sigma(1+k_{isc}/k_d)]$, where k_{isc} and k_d are the rate constants for intersystem crossing to the triplet state and relaxation to the ground state, respectively. Furthermore, the expression for CRM can be simplified under saturated ($I_e \gg I_s$) and unsaturated ($I_e \ll I_s$) conditions

$$CRM|_{I_e \gg I_s} \sim \kappa k_{rad} \tag{2a}$$

$$CRM|_{I_e \ll I_s} \sim \kappa\phi\sigma I_e \tag{2b}$$

According to Eq. 2, CRM enhancement by plasmonic structures (e.g. nanoantennas) consists of three contributions—local increase in the excitation intensity I_e, local increase in the radiative emission k_{rad} or quantum efficiency ϕ of enclosed fluorophores, and modification of the collection efficiency κ.

#175459 - $15.00 USD Received 6 Sep 2012; revised 30 Nov 2012; accepted 1 Dec 2012; published 21 Dec 2012

The enhancement of quantum efficiency (QE) can be expressed as [9]

$$f_\phi = \frac{f_{rad}}{(1-\phi_o)+\phi_o f_{Purcell}} \tag{3}$$

where ϕ_o is the native QE, and f_{rad} is the ratio of the k_{rad} values calculated with (denoted with ') and without the antenna. The ratio

$$f_{Purcell} = \frac{k'_{tot}}{k_{tot}}$$

is known as the Purcell factor, which represents the change in spontaneous emission rate of a perfect dipole [17]. According to Eq. 3, the modified QE varies dramatically based upon the native QE of the fluorophore. Here, we use tryptophan (Trp) as the model fluorophore, whose native quantum efficiency is $\phi_o = 13\%$ [1]. Trp has maximum absorption near 266 nm and peak emission near 340 nm. It is noted that radiation only into the substrate is used in our calculations, which corresponds to typical epifluorescence setup through a glass substrate [18], resulting in the calculation of an effective quantum efficiency. Thus, ϕ_o of tryptophan becomes 8% [19].

The net enhancement (NE) of fluorescence can be described as

$$NE|_{I_e \gg I_s} = f_\kappa f_{rad} \tag{4a}$$

$$NE|_{I_e \ll I_s} = f_\kappa f_I f_\phi \tag{4b}$$

where f_I is the excitation enhancement and f_κ is the enhancement in collection efficiency which is assumed equal to 1. The impacts of different antenna structures on κ will be considered by comparing the far-field radiation profiles.

In summary, five important parameters have been introduced. Excitation enhancement (f_I) is often used as the primary metric in the design and analysis of plasmonic structures. The Purcell factor ($f_{Purcell}$) is the increase in total energy emitted by an ideal dipole, which is inversely related to its increase in lifetime. The radiative enhancement (f_{rad}) stands for the fluorescence enhancement under saturated condition. QE enhancement (f_ϕ) is a parameter that relates to the radiation efficiency of the fluorophore. NE quantifies the net fluorescence enhancement, including excitation and emission components. In the following section, these parameters will be used as figures of merit in order to analyze the influence of nanoantenna design on UV fluorescence.

The three nanoantenna structures considered in this paper are depicted in Fig. 2, including the plan views and cross sections of (a) dipole antenna, (b) bull's eye aperture and (c) aperture array. The structures are assumed to be supported by a semi-infinite glass (SiO_2) substrate and covered by water. The active region, where the enhanced local field interacts with the fluorophore, is shown in zoom-in image in Fig. 2 extending just 10 nm above the glass substrate. Dielectric constants of aluminum, water and glass are incorporated via the dielectric constant obtained from handbook data [20].

Three-dimensional electromagnetic simulation is performed using Lumerical FDTD Solutions. Antisymmetric and symmetric boundaries are used along the x and y directions according to the symmetry of the structure and the source, which reduces the calculation and memory overhead without sacrificing resolution. Perfectly matched layers (PML) are used on the other boundaries. The grid size is $1\times1\times1$ nm^3 for the dipole antenna and $2\times2\times$ 2 nm^3 for the bull's eye and hole array. In order to calculate the excitation enhancement factor f_I, a plane wave with unit amplitude (1 V/m) is introduced inside the substrate, which normally illuminates the structures from the bottom. Average enhancement is calculated by integrating the total intensity within a 10 nm thick monitor covering the active region, and dividing by the integrated

#175459 - $15.00 USD Received 6 Sep 2012; revised 30 Nov 2012; accepted 1 Dec 2012; published 21 Dec 2012

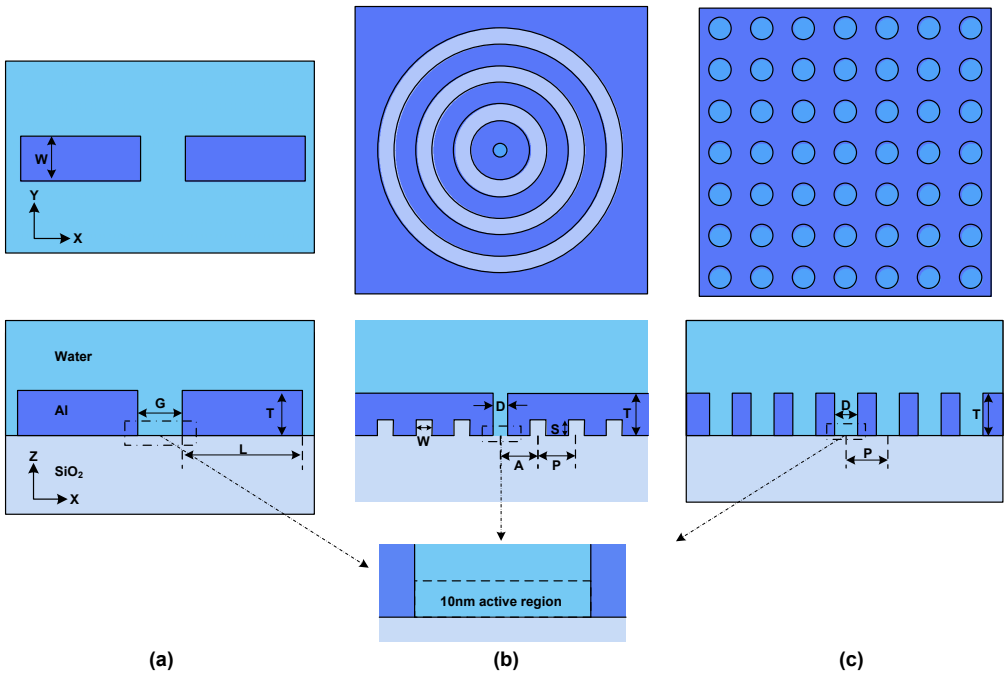

Fig. 2. Plan view along the interface and *xz* cross-section of (a) dipole antenna, (b) bull's eye aperture and (c) aperture array. The active region with 10 nm thickness is also shown.

intensity within the same volume but in the absence of the metallic structures. For the emission calculations, the analysis of the FDTD results rely on the fact that, for an atomic dipole transition that can only occur through radiation, the quantum mechanical decay rate in an inhomogeneous environment can be related to the classical power radiated by the dipole in the same environment [21]. Specifically, we can relate every rate constant to the corresponding power, such as

$$\frac{k_{rad}}{k_{rad}+k_{nr}} = \frac{P_{rad}}{P_o}$$

where P_{rad} and P_o are the radiative and total emission power of a dipole. Therefore, an electric dipole with unit amplitude (1 V/m) (at 340 nm) is positioned at the center of active region. The radiative emission is calculated as the transmission through monitors around the structure, while the total emission is calculated as the transmission through monitors around the dipole. Then the radiative enhancement (f_{rad}) and Purcell factor ($f_{Purcell}$) can be obtained by dividing the corresponding emission with those without the antenna structure. Calculations are performed for *x*, *y*, and *z* dipole orientations, and the reported enhancements are an average across these orientations. Then QE enhancement and NE can be calculated according to Eq. 3 and 4a.

3. Results and discussion

3.1. Dipole antenna design

There are four geometrical parameters determining the response of the dipole antenna, as shown in Fig. 2. The arm length L defines the antenna resonance wavelength, while the gap distance G affects the coupling between the two arms. In our studies, we fix both thickness T and width W of each arm at 30 nm for simplicity, and vary gap size ($20 \leq G \leq 50$ nm) and arm length ($20 \leq L \leq 180$ nm).

#175459 - $15.00 USD Received 6 Sep 2012; revised 30 Nov 2012; accepted 1 Dec 2012; published 21 Dec 2012

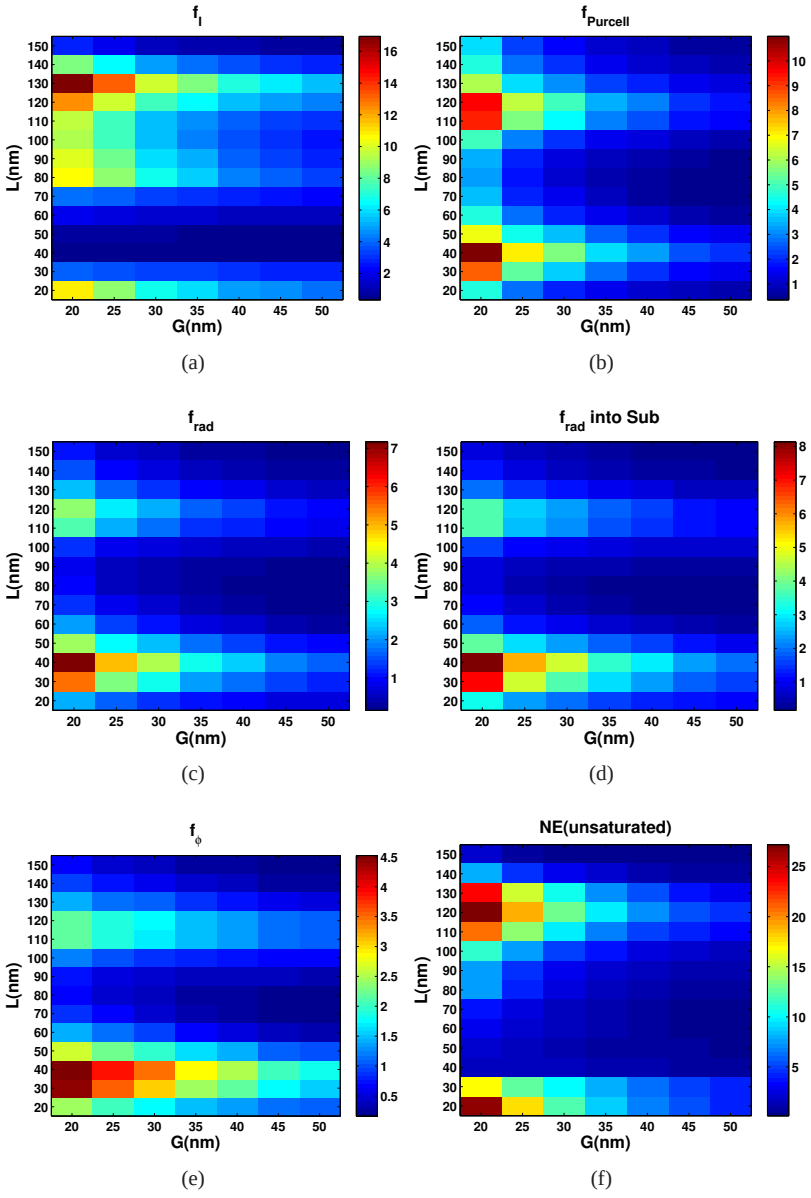

Fig. 3. Heat maps of (a) excitation enhancement (f_I), (b) Purcell factor ($f_{Purcell}$), (c) and (d) radiative enhancement (f_{rad}), (e) QE enhancement (f_ϕ) and (f) NE (unsaturated) for an Al dipole antenna versus gap size (G) and arm length (L). (T=30 nm, W=30 nm).

#175459 - $15.00 USD Received 6 Sep 2012; revised 30 Nov 2012; accepted 1 Dec 2012; published 21 Dec 2012

Figure 3 shows the 2-D enhancement maps of six antenna performance metrics versus L and G. Peaks in both excitation and emission enhancement occur under resonance conditions determined by the arm length, whereas the gap size controls the level of enhancement. As expected, smaller gap size generates higher enhancement due to the stronger coupling between the arms. From the map of excitation enhancement in Fig. 3(a), there are three resonances at the excitation wavelength, for arm lengths L=20 nm, 80 nm and 130 nm. The field intensity distributions (not shown) verify that these correspond to different resonance orders. Furthermore, peak enhancement increases with the arm length, which agrees with previous research [22], but it decreases at the fourth resonance (not shown here) due to the increase of material absorption. The highest excitation enhancement is $\sim$17 at the third resonance (when G=20 nm).

From the maps of emission enhancement in Fig. 3(b), 3(c), 3(d) and 3(e), the first and second peak values are at L=40 nm and 120 nm, which are shifted to longer arm length due to the longer emission wavelength of the dipole (340 nm compared to 266 nm). Comparing the peak enhancements at the two emission resonances, the Purcell factor is relatively unaffected by the arm length (maximum $f_{Purcell}$ is $\sim$11 when G=20 nm and L=40 nm), but the radiative enhancement factor (f_{rad}) has a lower peak value at the longer arm length. This behavior implies that the non-radiative emission increases with increase of the volume of metallic structure, which in turn gives the lower peak enhancement of QE at the longer arm, as shown in Fig. 3(e) (maximum f_ϕ is $\sim$4.5 when G=20 nm, L=30 nm). The net enhancement (NE) in Fig. 3(f) is the product of f_I and f_ϕ, and reaches maximum values of $\sim$27 at both the first (L=20 nm, G=20 nm) and second (L=120 nm, G=20 nm) resonance, where QE enhancement is greater for the shorter antenna. It should be noted again that only the radiative enhancement into the substrate is used to calculate f_ϕ and NE, but due to the finite thickness of the antenna, some radiation escapes into the upper halfspace.

In the above analysis, the radiation pattern was not considered (i.e. $f_\kappa = 1$). The far-field radiation patterns of structures corresponding to the first (L=20 nm, G=20 nm) and second (L=120 nm, G=20 nm) peak NE, calculated for an x-polarized electric dipole in the active region, are shown in Fig. 4(a). The patterns are indicative of dipole and quadrupole resonances, because the two structures are close to the corresponding order of emission resonance. The radiation of the first resonance has a prominent main lobe along the z direction (270°) with a divergence angle of $\pm$55°, while radiation from the second resonance has two strong side lobes around $\pm$50° with respect to the z direction, each side lobe with divergence angle around $\pm$15°. The spatial cross-section distributions of $|E|^2$ for the two resonance modes are also shown in Fig. 4(b) and 4(c), respectively. A logarithmic scale is used to allow a greater dynamic range of field intensity to be displayed. The two distinct resonance modes are clearly seen by inspecting the number of nodes in the antenna arms.

3.2. Bull's eye antenna design

The bull's eye antenna has more a complicated structure compared to the dipole antenna, which involves six geometrical parameters shown in Fig. 2. Fortunately, most of of parameters can be approximately related to the groove pitch P through design criteria [23]. In addition, the hole diameter (D) defines the environment around the fluorophore, and has an influence on emission enhancement somewhat independent from the other parameters. The depth (S) and width (W) of the grooves can further modify the optical response through groove modes [24], but these don't change the working mechanism of the bull's eye structure, which relies on constructive interference at the central hole of standing waves emitted by the independent grooves [25]. Therefore, we fix the depth and width as S =20 nm and W =60 nm to remove the effect of the groove mode for simplicity. The thickness of the structure (T) is set to 100 nm. The number of grooves is set as 3 to reduce memory and computational time requirements.

#175459 - $15.00 USD Received 6 Sep 2012; revised 30 Nov 2012; accepted 1 Dec 2012; published 21 Dec 2012

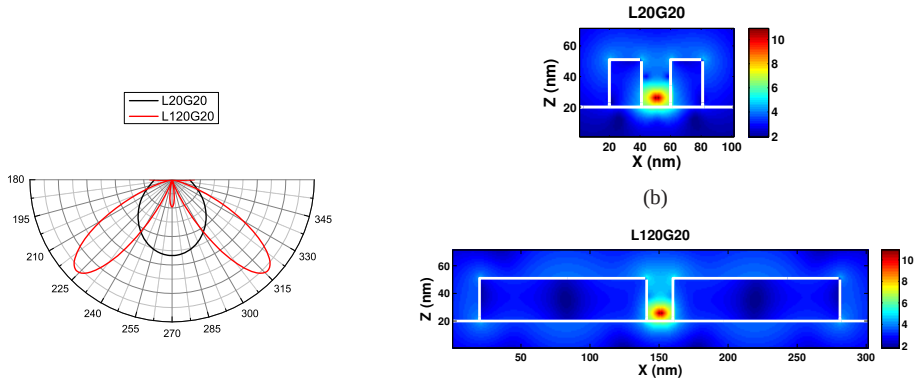

Fig. 4. (a) Far-field angular radiation patterns of structures corresponding to the first (L=20 nm) and second (L=120 nm) peak NE for the dipole antenna. (b), (c) Corresponding spatial distribution of $|E|^2$ in xz cross section . An x-polarized electric dipole with 340 nm wavelength is placed in the center of the active region. (G=20 nm, W=30 nm, T=30 nm).

Maps of the different figures of merit are generated by changing the hole size ($40 \leq D \leq 100$ nm) and pitch ($100 \leq P \leq 320$ nm), as shown in Fig. 5. These maps have similar features to those of the dipole antenna: peaks in both excitation and emission enhancements occur under resonant conditions, determined by the pitch (P), while the hole size (D) affects the level of enhancement. The map of f_I in Fig. 5(a) has first, second and third resonance peaks at P=140 nm, 200 nm and 300 nm. The larger pitch produces the higher enhancement due to the greater area for light collection. The maximum excitation enhancement is $\sim$61 at the third resonance with D=50 nm. The maps of emission enhancement in Fig. 5(b), 5(c), 5(d) and 5(e) show the first and second peak values around P=180 nm and 280 nm, which are also shifted due to the difference in wavelengths between emission and excitation. The map of NE under unsaturated condition in Fig. 5(f) also exhibits three peaks, with values of $\sim$91, 118 and 188 at P=140 nm, 200 nm and 300 nm, respectively (at D=50 nm), which follows exactly the resonances of f_I because of the dominate effect of f_I over f_ϕ.

The far-field radiation patterns are also considered, as shown in Fig. 6(a). Three patterns corresponding to the three peak values of NE are plotted. The pattern of the first peak ($P140D50$) has two comparatively small side lobes, each with divergence angle of $\pm 15^\circ$, because the pitch corresponds to the excitation resonance rather than the emission resonance. By contrast, the other two patterns are from structures that are close to emission resonance, and show the features of first order resonance (a main lobe along z with a divergence angle of $\pm 5^\circ$) and second order of resonance (two strong side lobes with divergence angles of $\pm 5^\circ$), respectively. The spatial distribution of $|E|^2$ for the three cases in cross-section at the glass interface is also shown in Fig. 6(b), 6(c) and 6(d), respectively. The resonance and off-resonance features can be clearly seen from the corresponding images.

It is worth comparing the bull's eye and dipole antennas. The bull's eye is an extended planar structure with much greater interaction cross-section, thus the excitation enhancement f_I is much higher for roughly the same active area. The round aperture in the bull's eye has an optimal size for the excitation and emission processes - about 50 nm for excitation and 70 nm for emission, which agree with previous studies [19] - whereas, enhancement will generally increase for the dipole antenna with decreasing gap. For the bull's eye, the peak values of f_{rad} into the substrate (Fig. 5(d)) are much larger than the total f_{rad} (Fig. 5(c)), because the

#175459 - $15.00 USD Received 6 Sep 2012; revised 30 Nov 2012; accepted 1 Dec 2012; published 21 Dec 2012

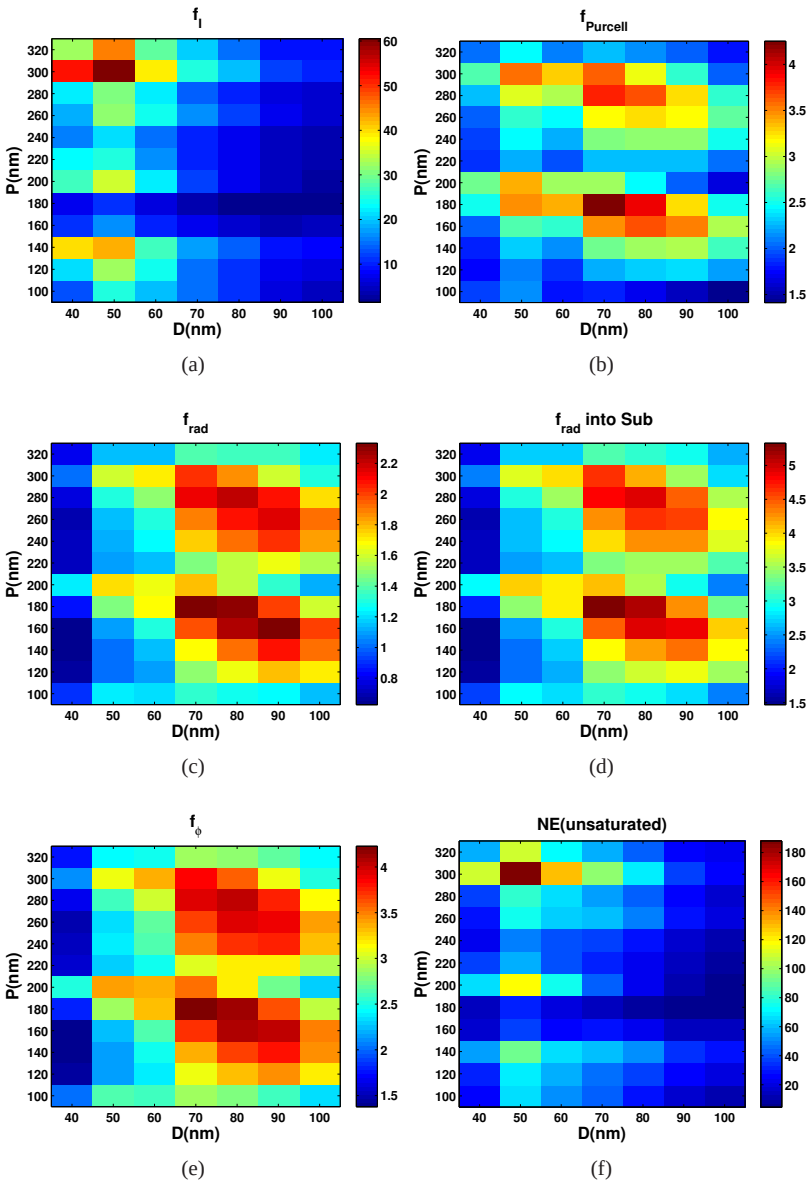

Fig. 5. Heat maps of (a) excitation enhancement (f_I), (b) Purcell factor ($f_{Purcell}$), (c) and (d) radiative enhancement (f_{rad}), (e) QE enhancement (f_ϕ) and (f) NE (unsaturated) for the bull's eye antenna versus hole size (D) and groove pitch (P). (A=P, W=60 nm, S =20 nm, T=100 nm)

#175459 - $15.00 USD Received 6 Sep 2012; revised 30 Nov 2012; accepted 1 Dec 2012; published 21 Dec 2012

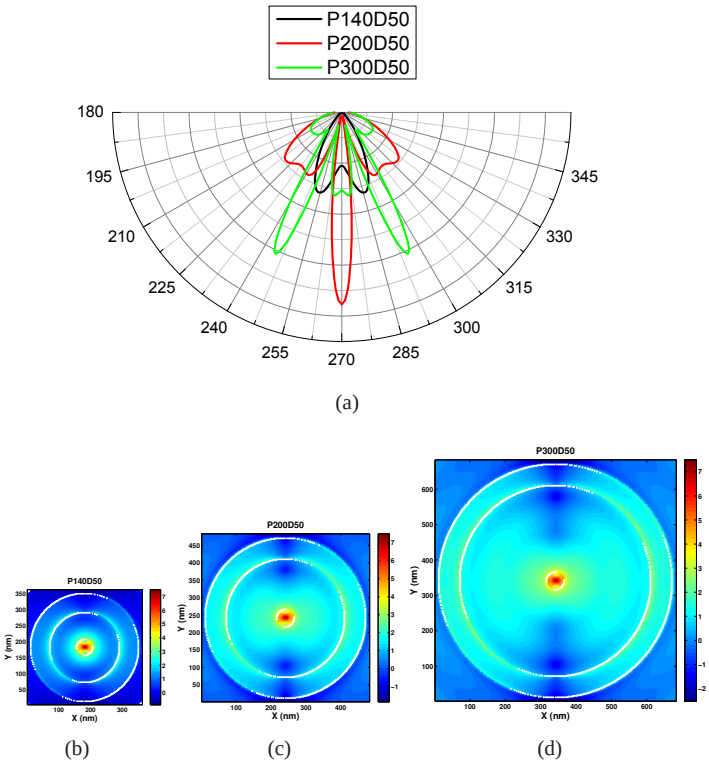

Fig. 6. (a) Far-field angular radiation patterns of the first (P=140 nm, off-resonance), the second (P=200 nm) and the third (P=300 nm) peak NE of bull's eye. (b), (c), (d) Corresponding spatial distribution of $|E|^2$ in the structure/glass interface (xy surface) of bull's eye. An x-polarized electric dipole with 340 nm wavelength is placed in the center of active region. (D=50 nm, A=P, W=60 nm, S=20 nm, T=100 nm)

thicker aperture strongly attenuates radiation into the upper halfplane. Furthermore, the bull's eye exhibits more directionality in emission due to constructive interference with scattering by the concentric grooves, and effect sometimes called "beaming" [26].

3.3. Aperture array design

If a fluorophore could be placed inside a specific aperture, an aperture array can be treated as a variation from the bull's eye with one central aperture surrounding by a square lattice of apertures instead of concentric grooves. Therefore, similar performance should be expected in terms of fluorescence excitation and emission. Again our analysis will be focused on period P and aperture size D as parameters. The thickness of the structure (T) is fixed at 100 nm. The total number of periods is set as 6 due to the limitation of memory and speed of FDTD simulation.

Maps of the figures of merit are generated by changing the aperture size ($40 \leq D \leq 100$ nm) and period ($100 \leq P \leq 320$ nm), and are shown in Fig. 7. Excitation enhancement shows resonance peaks near same regions as the bull's eye, but with much smaller enhancement values (maximum $f_I \sim 23$). A more obvious difference can be seen from emission enhancement in Fig. 7(b), 7(c), 7(d) and 7(e). The influence of the period is less distinct, which implies that there's a weaker interaction between the central and nearby apertures than there is between a

#175459 - $15.00 USD Received 6 Sep 2012; revised 30 Nov 2012; accepted 1 Dec 2012; published 21 Dec 2012

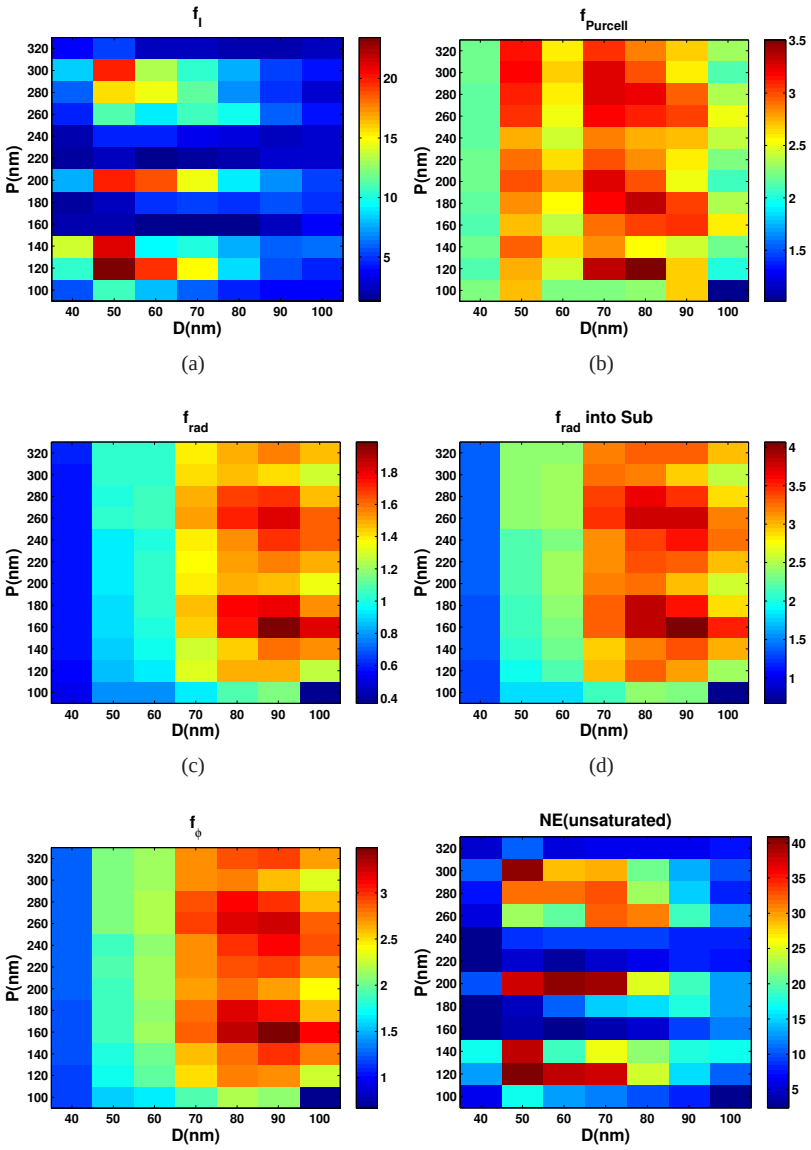

Fig. 7. Heat maps of (a) excitation enhancement (f_I), (b) Purcell factor ($f_{Purcell}$), (c) and (d) radiative enhancement (f_{rad}), (e) QE enhancement (f_ϕ) and (f) NE (unsaturated) for an aperture array versus aperture size (D) and period (P). (T=100 nm)

#175459 - $15.00 USD Received 6 Sep 2012; revised 30 Nov 2012; accepted 1 Dec 2012; published 21 Dec 2012

central aperture and concentric grooves. Therefore, the emission enhancement of the aperture array is closer to that of a single aperture, where the aperture size D is the dominant factor. The emission figures of merit $f_{Purcell}$, f_{rad} and f_{ϕ} have similar features, with maximum enhancements $\sim$4, for D $\sim$80 nm. These results are very close to those from a single aperture reported before [19] and obtained from a different simulation method, which further validates our analysis. The map of NE under unsaturated conditions exhibits three peaks, with values $\sim$41, 37 and 40 at P=120 nm, 200 nm and 300 nm, respectively, for D=50 nm, which follow the dominant excitation resonance. The stronger excitation enhancement due to the collective SPP resonance makes the NE of an aperture array stronger than that of single aperture.

The far-field angular radiation patterns from the aperture array are shown in Fig. 8(a). The patterns for the near resonant cases ($P200D50$ and $P300D50$) have distinct directional peaks on broad non-directional backgrounds, implying some interaction between apertures, while the off-resonance ($P120D50$) case exhibits a broad non-directional pattern, suggesting reduced inter-aperture interaction. The spatial distributions of $|E|^2$ at the glass interface for the three cases is also shown in Fig. 8(b), 8(c) and 8(d), respectively, showing that there is no interaction between apertures in Fig. 8 (b), while weak interaction can be found in Fig. 8(c) and 8(d).

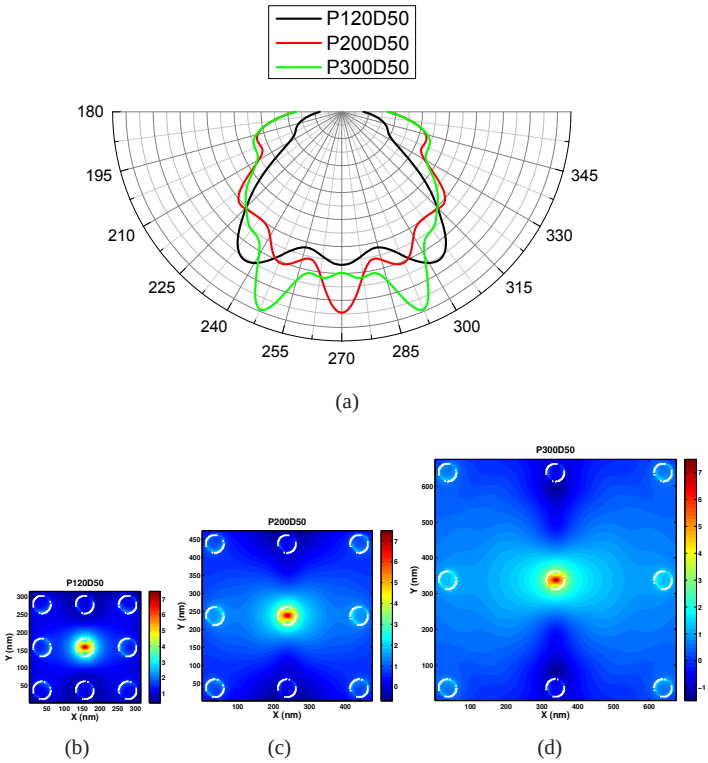

Fig. 8. Far-field angular radiation patterns of the first (P=120 nm, off-resonance), the second (P=200 nm) and the third (P=300 nm) peak NE of aperture array. (b), (c), (d) Corresponding spatial distribution of $|E|2$ in the structure/glass interface (xy surface) of aperture array. An x-polarized electric dipole with 340 nm wavelength is placed in the center of active region. (D=50 nm, T=100 nm)

#175459 - $15.00 USD Received 6 Sep 2012; revised 30 Nov 2012; accepted 1 Dec 2012; published 21 Dec 2012

3.4. *Performance comparison*

After the analysis of the three antenna structures, it is helpful to compare their performance. The maximum enhancement values are listed in Table 1.

Table 1. Comparison of performance metrics for the three nanoantennas

Structure	f_I	$f_{Purcell}$	f_{rad}	f_{rad} into Sub	f_ϕ	NE
Dipole	16.9	11.0	7.2	8.1	4.5	27.2
Bull's eye	60.5	4.3	2.3	5.3	4.2	188.0
Aperture array	23.4	3.5	2.0	4.1	3.5	40.9

* The numerical value listed for each metric is the peak value based upon optimal geometrical parameters.

For excitation enhancement (f_I) under plane wave illumination, the bull's eye gives the best performance ($\sim$61) due to its large concentrating structure. While comparing the structures based upon plane wave illumination might be appropriate for nanoantenna arrays, if single structures are to be compared, then focused illumination needs to be considered. For example, comparing the dipole and bull's eye structures under the conditions of maximal f_I, one might use focused illumination of diameters 280 nm and 1.8 μm, respectively. Assuming the same power in each beam, then the intensity in the gap of the dipole antenna would be about 700$\times$ the intensity incident on the bull's eye, for which the intensity within the central aperture of bull's eye remains as 60.5$\times$ incident. This comparison is simply a statement that, within the diffraction limit, focusing via conventional imaging is more efficient than plasmonic focusing. The dipole antenna produces the highest emission enhancement with $f_{Purcell} \sim$11, $f_{rad} \sim$7, and $f_\phi \sim$4.5, due to it's favorable gap structure.

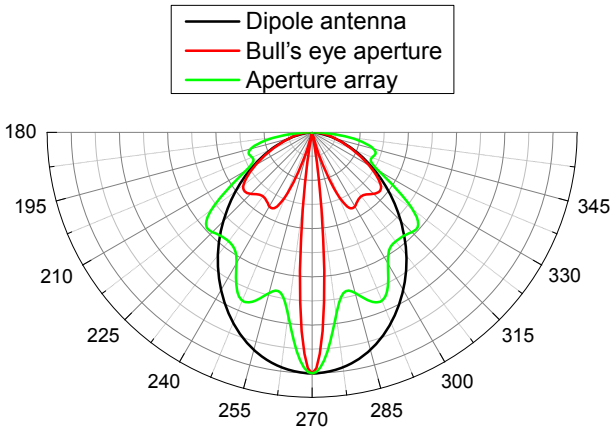

Fig. 9. Far-field angular radiation patterns of three nanoantennas. Only the first order emission resonances are considered and patterns are normalized. An *x*-polarized electric dipole with 340 nm wavelength is placed in the center of active region.

The far-field angular radiation patterns of the first order of emission resonance from three structures is shown in Fig. 9. The patterns are normalized for comparison. The bull's eye antenna has the most directionality due to its extended structure with strongly interacting concentric grooves.

#175459 - $15.00 USD Received 6 Sep 2012; revised 30 Nov 2012; accepted 1 Dec 2012; published 21 Dec 2012

4. Conclusion

In conclusion, three plasmonic antenna structures for UV fluorescence enhancement are numerically studied by comparing five performance metrics: excitation enhancement (f_I), Purcell factor ($f_{Purcell}$), radiative enhancement (f_{rad}), QE enhancement (f_ϕ) and NE. The 2-D maps of performance metrics versus geometrical parameters are generated in order to clarify the influence of structure parameters. The far-field radiation patterns are also considered. All three structures present similar features that peak enhancement of the excitation and emission processes occurs under resonant conditions, determined by arm length for dipole antenna and pitch for other two structures. Furthermore, distinct differences are observed across the structures. The bull's eye aperture and aperture array produces higher enhancements due to their extended planar structure with much greater physical interaction cross-section with incident light. Decrease of gap size of dipole antenna will increase the enhancement of excitation and emission, while the round apertures in the bull's eye and aperture array have an optimal size for the excitation ($\sim$ 50 nm) and emission ($\sim$ 70 nm) processes. Due to the favorable gap structure, the dipole antenna produces higher Purcell factor ($f_{Purcell} \sim$11), radiative enhancement ($f_{rad} \sim 7$) and QE enhancement ($f_\phi \sim$4.5). The thicker structures of bull's eye and aperture array effectively suppress radiation in the direction away from the substrate, which is preferable for an epifluorescence setup. The far-field radiation of the bull's eye aperture has the most directionality due to constructive interference with scattering by the concentric grooves. The aperture array has the least directionality due to the weak interaction between central and neighboring apertures.

Acknowledgements

This work was supported by NSF MRSEC grant DMR 1121252.

#175459 - $15.00 USD Received 6 Sep 2012; revised 30 Nov 2012; accepted 1 Dec 2012; published 21 Dec 2012